

PAPER



Cite this: *J. Mater. Chem. C*, 2019,
7, 13829

Received 17th August 2019,
Accepted 10th October 2019

DOI: 10.1039/c9tc04561a

rsc.li/materials-c

Electron beam-induced morphology transformations of Fe₂TiO₅ nanoparticles

Sijie Li, Junyu Zhong, Zhipeng Cui, Qingye Zhang, Meng Sun and Yiqian Wang *

Iron(III) titanium oxide, Fe₂TiO₅, is attracting growing interest as a promising candidate for solar-energy and electrochemistry applications. In this paper, we studied the effects of electron-beam irradiation on the morphology and microstructure of Fe₂TiO₅ nanoparticles (NPs) produced by a solvothermal method, with or without the addition of polyvinyl-pyrrolidone (PVP). For the Fe₂TiO₅ NPs produced without adding PVP, their structure and morphology show no obvious changes under electron beam irradiation. However, for the Fe₂TiO₅ NPs produced with PVP, they undergo three distinct stages of morphological evolution under the electron beam irradiation, namely, layer exfoliation, local pulverization, and amorphization. The different behaviors are attributed to the fact that PVP can generate oxygen vacancies in Fe₂TiO₅. The thermal effect and knock-on collision caused by the electron beam play a dominant role in the morphological changes of Fe₂TiO₅ NPs produced with PVP. Our results provide insights into the morphological evolution of polymetallic oxides under electron beam irradiation.

1. Introduction

Fe₂TiO₅, an n-type semiconductor oxide containing binary metal elements, has attracted much attention in recent years. It combines the advantages of two metal oxides, TiO₂ and Fe₂O₃, and has potential applications in solar water splitting,^{1–3} photo-degradation,⁴ Li-ion battery anodes^{5,6} and gas sensors.⁷

In the past two decades, researchers have devoted great effort in the preparation of Fe₂TiO₅ nanoparticles (NPs).^{5–9} Various methods have been adopted to fabricate Fe₂TiO₅ NPs, such as hydrothermal processes,^{5,6} solid state reactions,^{7,8} and sol-gel methods.⁹ Moreover, polyvinyl-pyrrolidone (PVP) has been used as a surfactant to control the size of Fe₂TiO₅ particles in the hydrothermal process.⁶ However, PVP has been found to produce oxygen vacancies in other oxide nanostructures such as TiO₂ NPs,¹⁰ CeO₂ NPs,¹¹ MoO₃ nanosheets,¹² and BiOBr nanosheets.¹³ Therefore, the exact role of PVP in the preparation process of Fe₂TiO₅ NPs needs to be further explored.

Fe₂TiO₅ has a pseudobrookite structure, a rare mineral structure known from the lunar mineral (Fe_{0.5}Mg_{0.5})Ti₂O₅,^{14,15} which is stable at high temperatures but metastable at room temperature.^{15,16} When the dimension of Fe₂TiO₅ is reduced to the nanoscale, its physical and chemical properties will change significantly, especially the structural stability. Such instability will become a major limitation for the application of Fe₂TiO₅ nanomaterials. The electron beam in transmission electron

microscopy (TEM) can be used to investigate the structural stability of Fe₂TiO₅ nanostructures. Many nanomaterials have been found to undergo various changes under electron beam irradiation, such as defect formation,¹⁷ mass loss,¹⁸ morphological evolution,^{19,20} phase transformation^{21–23} along with the nucleation and formation of some metallic NPs.^{24–27} For single metal oxides^{17,19–21,24,25} under electron beam irradiation, the microstructural evolution behaviors have been extensively studied. However, for the polymetallic oxides under the electron beam irradiation, the microstructure evolution is complicated due to their intricate structures. Some polymetallic oxides are reported to undergo a structural phase transformation under electron beam irradiation, *i.e.* the emergence of a second orthorhombic phase in BiEuWO₆,²² and a new modulated structure in BiMnO₃.²³ The other polymetallic oxides are found to produce metallic NPs on their surfaces under electron beam irradiation such as Ag-based oxides (Ag₂WO₄ and Ag₂CrO₄)²⁶ and Bi-based oxide (NaBiO₃).²⁷ However, to the best of our knowledge, no report has been published on the microstructural evolution of Fe₂TiO₅ nanostructures under electron beam irradiation. Therefore, it is necessary to investigate the microstructural changes of Fe₂TiO₅ nanostructures under the electron beam, and explore the evolution mechanism.

In this work, we investigate the role of PVP in the synthesis of Fe₂TiO₅ NPs and the effect of electron beam irradiation on the stability of the Fe₂TiO₅ NPs produced with or without the addition of PVP. This shows that the addition of PVP can lead to the formation of oxygen vacancies in Fe₂TiO₅ NPs, which results in the morphological changes of Fe₂TiO₅ NPs under electron beam irradiation. The microstructural evolution mechanism for Fe₂TiO₅ NPs is also explored.

College of Physics & State Key Laboratory, Qingdao University, No. 308 Ningxia Road, Qingdao, 266071, People's Republic of China. E-mail: yqwang@qdu.edu.cn; Tel: +86-532-83780318

2. Experimental

2.1. Chemical reagents

N,N-Dimethylformamide (DMF, C₃H₇NO, 99.0%), isopropanol (IPA, C₃H₈O, 99.0%), iron(III) acetylacetonate (Fe(acac)₃, C₁₅H₂₁FeO₆, 98.0%), tetrabutyl titanate (TBT, Ti(OC₄H₉)₄, 98.0%), and polyvinylpyrrolidone (PVP, (C₆H₉NO)_{*n*}, K-30) were purchased from Sinopharm Chemical Reagent Company Limited. All the chemicals are of analytical grade and were used as purchased without further purification.

2.2. Preparation of Fe₂TiO₅ NPs

Fe₂TiO₅ NPs were prepared by a simple solvothermal method, following a slightly adapted procedure.⁶ At first, 10 mL of DMF was added into 30 mL of IPA to form a homogeneous solution under vigorous stirring at room temperature. Then, 0.50 mL of TBT and 1.02 g of Fe(acac)₃ (molar ratio: 1 : 2) were added into the above solution, and stirred until complete dissolution. The obtained red solution was transferred into a 100 mL Teflon-lined stainless steel autoclave and maintained at 180 °C for 20 h to obtain the precursor. Afterwards, the reddish brown precursor was collected by centrifugation and washed several times with deionized water and ethanol, and dried at 60 °C overnight. Finally, the obtained precipitates were further annealed in air at 550 °C for 3 h, and the resultant product was referred to as FTO NPs. To study the effect of PVP on the size, morphology, and structure of Fe₂TiO₅ NPs, we also prepared the Fe₂TiO₅ NPs using the same procedure with the only difference of adding PVP in the first step (addition of 0.50 g of PVP into the mixed solution of 10 mL of DMF and 30 mL of IPA). The resultant product was named FTO-PVP NPs.

Specimens for TEM observations were prepared by dropping 10 μL of the Fe₂TiO₅ ethanol suspensions onto ultrathin holey-carbon-coated Cu grids and drying under an infrared lamp.

2.3. Material characterization

The crystal structure of the NPs was investigated by X-ray diffraction (XRD, Rigaku SmartLab) with Cu-Kα₁ radiation ($\lambda = 1.5406 \text{ \AA}$) with 2θ ranging from 15° to 80°. The nitrogen adsorption-desorption tests were carried out on an automatic volumetric sorption analyzer (NOVA 1100, Quantachrome, USA) at 77 K. The Brunauer-Emmett-Teller (BET) method was used to calculate the specific surface area and total pore volume of the products. The Barrett-Joyner-Halenda (BJH) method was utilized to obtain the pore size distribution from the desorption branches of the isotherms. X-ray photoelectron spectroscopy (XPS) was performed on a Thermo Scientific ESCALAB 250Xi instrument with monochromatic Al Kα radiation ($h\nu = 1486.6 \text{ eV}$) at an ultrahigh vacuum (below 10⁻⁸ Pa). The binding energies were calibrated using the C 1s peak (284.5 eV) as a reference. The Fourier transform infrared reflection (FT-IR) spectra of the samples were recorded on a Fourier transform infrared spectrometer (Thermo Scientific Nicolet iS50).

Bright-field (BF) imaging, selected-area electron diffraction (SAED) and high-resolution TEM (HRTEM) examinations were carried out on a JEOL JEM2100F electron microscope operated

at 200 kV. The chemical composition of the Fe₂TiO₅ NPs produced with and without the addition of PVP was analyzed by X-ray energy-dispersive spectroscopy (EDS) installed on an electron microscope. Electron energy-loss spectroscopy (EELS) spectra of the FTO NPs and FTO-PVP NPs before and after the electron beam irradiation were acquired using a JEM ARM200CF transmission electronic microscope, operating at 200 kV.

3. Results and discussion

XRD was used to investigate the effect of PVP on the crystal structure of the synthesized products. Fig. 1 shows the XRD patterns obtained from FTO NPs and FTO-PVP NPs, respectively. Both patterns can be indexed with an orthorhombic phase of Fe₂TiO₅ (JCPDS no.: 41-1432).⁶ The diffraction peaks at 18.0°, 25.5°, 32.5°, 36.5°, 37.3°, 45.9° and 48.7° correspond to the (200), (101), (230), (301), (131), (430) and (002) planes of Fe₂TiO₅, respectively. No apparent differences can be found in the position and intensity of the diffraction peaks in both patterns. In addition, no miscellaneous peaks are observed in both patterns. Thus, we conclude that the addition of PVP does not change the crystal structure and crystallinity of FTO-PVP NPs.

To obtain further information about the size and morphology of the FTO NPs and FTO-PVP NPs, extensive TEM examinations were carried out. To avoid the influence of electron beam irradiation on the particle size of the two specimens, the TEM images were taken at a low electron beam current density ($\sim 15 \text{ pA cm}^{-2}$). Fig. 2a and c show typical BF TEM images of the two samples, and their corresponding SAED patterns are displayed as insets in the lower left corners of the images. Both SAED patterns demonstrate a polycrystalline nature of the particles, which can be indexed using an orthorhombic phase of Fe₂TiO₅ (space group: *Bbmm*, $a = 9.797 \text{ \AA}$, $b = 9.981 \text{ \AA}$, and $c = 3.730 \text{ \AA}$). From the typical BF TEM images, it can be seen that all the NPs have irregular shapes and uneven sizes. To get a reliable size distribution of the two samples, we recorded more than 100 NPs of each sample and carried out a statistical analysis. Fig. 2b and d show the statistical size distribution

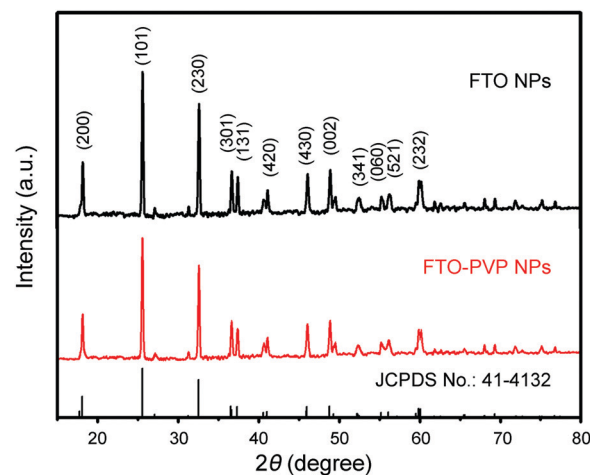


Fig. 1 XRD patterns of FTO NPs (black) and FTO-PVP NPs (red).

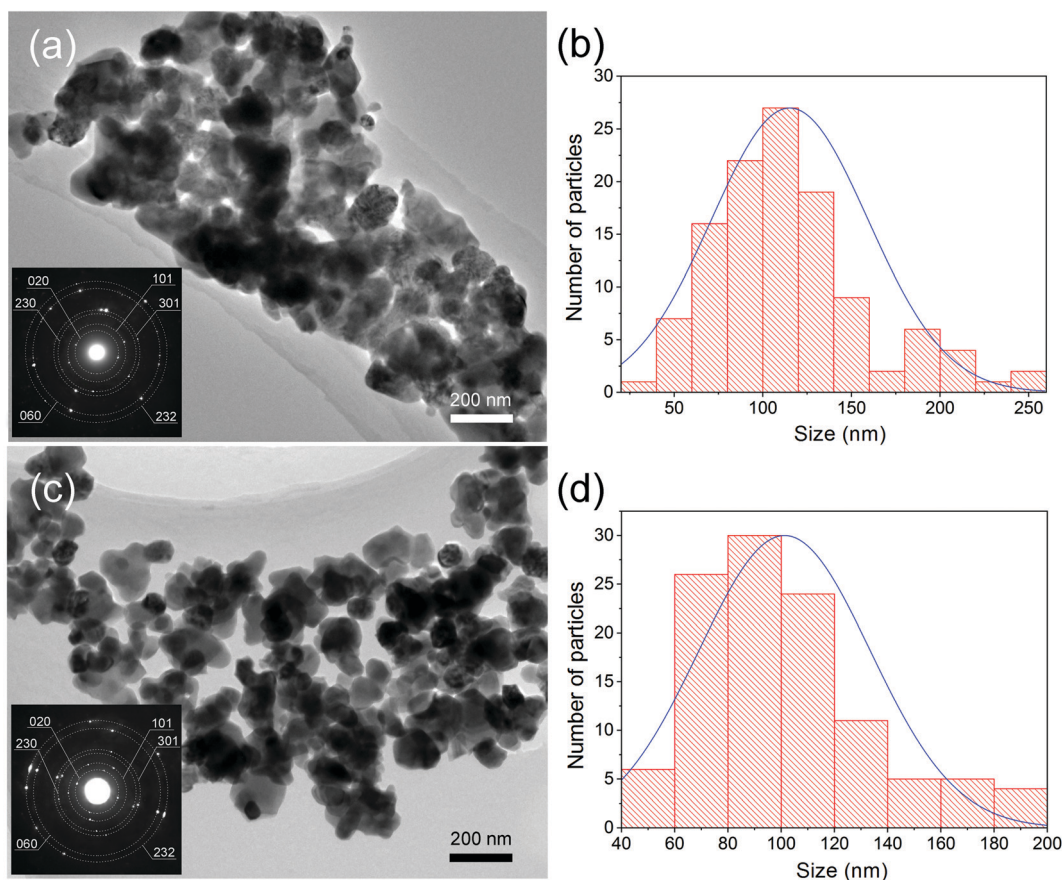


Fig. 2 Typical BF TEM images of FTO NPs (a) and FTO-PVP NPs (c). Insets show the corresponding SAED patterns. Statistical size distributions of FTO NPs (b) and FTO-PVP NPs (d).

for FTO NPs and FTO-PVP NPs, respectively. The FTO NPs range from 40 nm to 280 nm with an average diameter of 120 nm, while the FTO-PVP NPs exhibit a narrow distribution from 40 to 200 nm with an average size of about 95 nm. By comparing the morphology and the size of the two samples, it is revealed that PVP slightly reduces the average particle size and narrows the size distribution of Fe_2TiO_5 NPs.

To explore the effect of PVP on the specific surface area and pore size of the as-synthesized Fe_2TiO_5 NPs, nitrogen

adsorption/desorption tests were carried out. Fig. 3a shows the N_2 adsorption–desorption isotherm curves of FTO NPs and FTO-PVP NPs. Both curves exhibit a type-III characteristic with hysteresis loops at a relative pressure P/P_0 of 0.85–1.0, which is one of the main characteristics for mesoporous materials.²⁸ From the pore size distribution curves shown in Fig. 3b, it can be seen that both samples have a similar pore size distribution with a dominant pore size of about 35 nm. Hence, both FTO NPs and FTO-PVP NPs possess a mesoporous

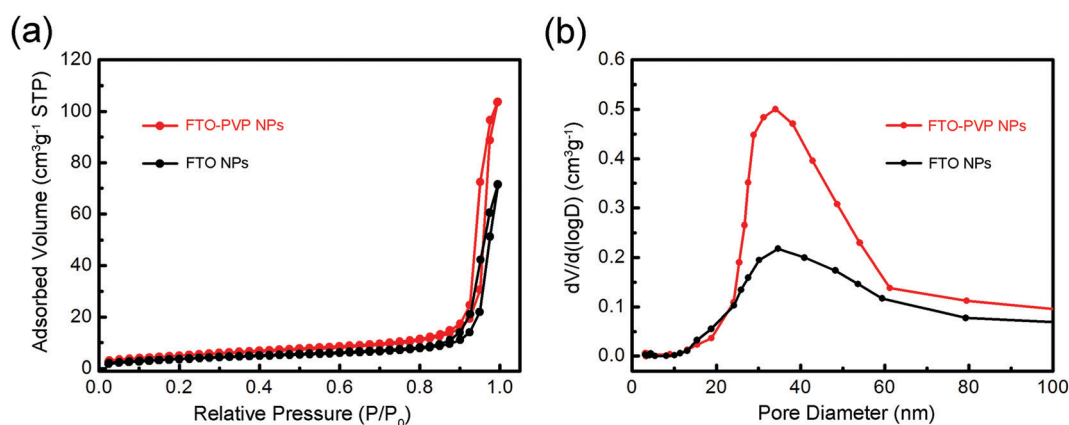


Fig. 3 Nitrogen adsorption–desorption isotherms (a) and pore size distribution curves (b) for FTO NPs (black) and FTO-PVP NPs (red).

structure. For FTO NPs, the BET surface area and the pore volume are calculated to be $13.627 \text{ m}^2 \text{ g}^{-1}$ and $0.1106 \text{ cm}^3 \text{ g}^{-1}$, respectively. For FTO-PVP NPs, the BET surface area is calculated to be $18.481 \text{ m}^2 \text{ g}^{-1}$ and the pore volume is $0.1605 \text{ cm}^3 \text{ g}^{-1}$, slightly larger than those of FTO NPs. Therefore, the addition of PVP does not change the mesoporous structure of Fe_2TiO_5 NPs, but affects their specific surface area and pore volume.

XPS analyses were performed to investigate the effect of PVP on the elemental composition, chemical bonding and corresponding valence states for FTO NPs and FTO-PVP NPs. In Fig. 4a, the peaks of Fe 2p, O 1s, Ti 2p and C 1s are shown, indicating the existence of Fe, Ti, O and C elements in both samples. The appearance of the C 1s signal can be attributed to the carbon contamination due to the ambient exposure of the products, which is usually found in oxides.²⁸ Fig. 4b shows the high-resolution XPS spectrum of O 1s, in which the lower binding-energy peak at 529.7 eV is assigned to intrinsic lattice oxygen, and the higher binding-energy peak at 533.0 eV is attributed to adsorbed oxygen.^{10,29} No significant difference can be found in O 1s spectra for the two samples. In Fig. 4c, two peaks at binding energies of 458.2 eV and 464.0 eV are associated with Ti $2p_{3/2}$ and Ti $2p_{1/2}$, respectively. The splitting binding energy between Ti $2p_{1/2}$ and Ti $2p_{3/2}$ core levels is ~ 5.8 eV, indicating a normal state of Ti^{4+} in the two samples.^{6,10,30} Except for the slight difference in peak intensity, no other difference is found between the two samples. For the Fe 2p spectra (Fig. 4d), the $2p_{3/2}$ and $2p_{1/2}$ peaks of FTO NPs are located at 711.0 eV and 724.7 eV, while a negative shift of about 0.3 eV is detected for

both $2p_{3/2}$ and $2p_{1/2}$ peaks in FTO-PVP NPs. In addition, small peaks with different intensities are found between the $2p_{3/2}$ and $2p_{1/2}$ peaks of FTO NPs and FTO-PVP NPs, as shown in the circled region. These small peaks are defined as satellite peaks, which can reflect the valence state of Fe.^{31,32} For FTO NPs, the satellite peak appears at 719.9 eV, suggesting that the valence state of Fe in the FTO NPs is Fe^{3+} .³¹ However, for the FTO-PVP NPs, no obvious satellite peak is observed, which is similar to that of Fe_3O_4 .³² In Fe_3O_4 , the absence of satellite peaks is attributed to the mixing of Fe^{2+} and Fe^{3+} .³² Moreover, the presence of Fe^{2+} also results in a negative shift of $2p_{3/2}$ and $2p_{1/2}$ peaks in Fe_3O_4 compared with Fe_2O_3 .³² Hence, it can be concluded that there is a small amount of Fe^{2+} in the FTO-PVP NPs. The presence of Fe^{2+} in FTO-PVP NPs inevitably accompanies the generation of oxygen vacancies. Therefore, the addition of PVP leads to the formation of oxygen vacancies in the Fe_2TiO_5 NPs.

To clarify whether organic residues exist in the synthesized and annealed products made with and without PVP, FT-IR spectroscopy was performed, as shown in Fig. 5. For the FTO NPs (Fig. 5a), the absorption bands at 425, 630 and 800 cm^{-1} are ascribed to pseudobrookite Fe_2TiO_5 ,³³ and no other bands are detected from 1000 cm^{-1} to 4000 cm^{-1} . However, for the FTO-PVP NPs (Fig. 5b), besides the absorption bands of Fe_2TiO_5 , two vibration bands at 1650 cm^{-1} and 1290 cm^{-1} are observed, which are attributed to the C=O stretching vibration and the C-N vibration in PVP.^{34,35} Thus, it can be concluded that the PVP molecules are present in both synthesized and annealed FTO-PVP NPs.

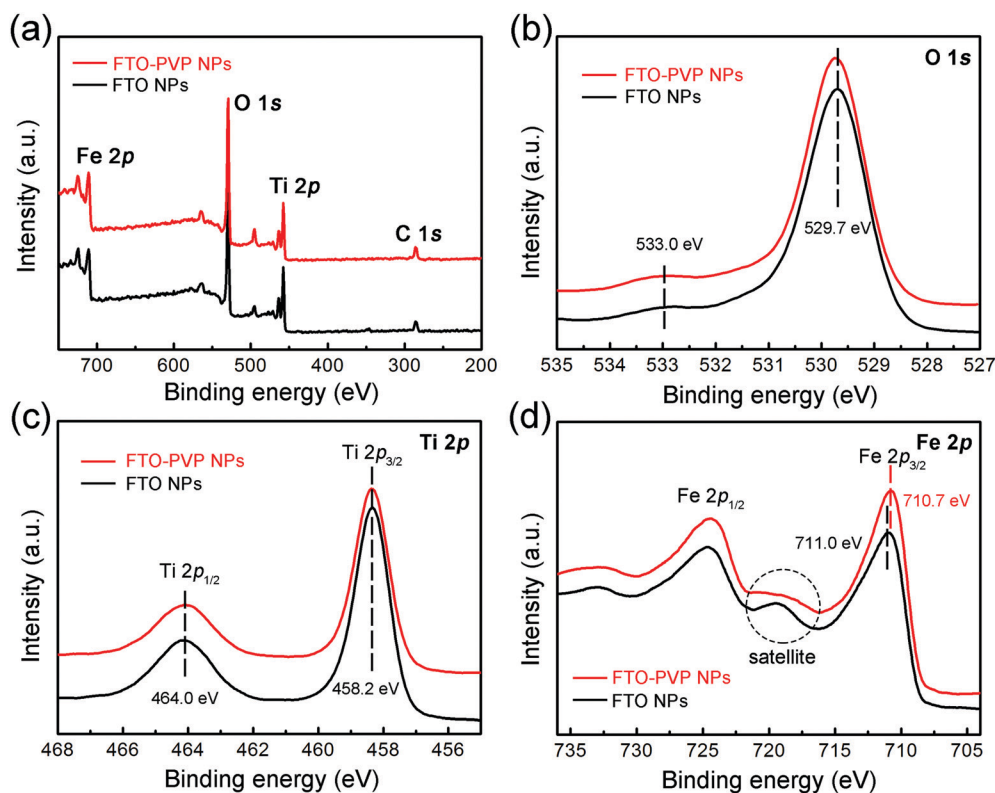


Fig. 4 XPS spectra of FTO NPs (black) and FTO-PVP NPs (red): (a) full scan, (b) O 1s, (c) Ti 2p and (d) Fe 2p.

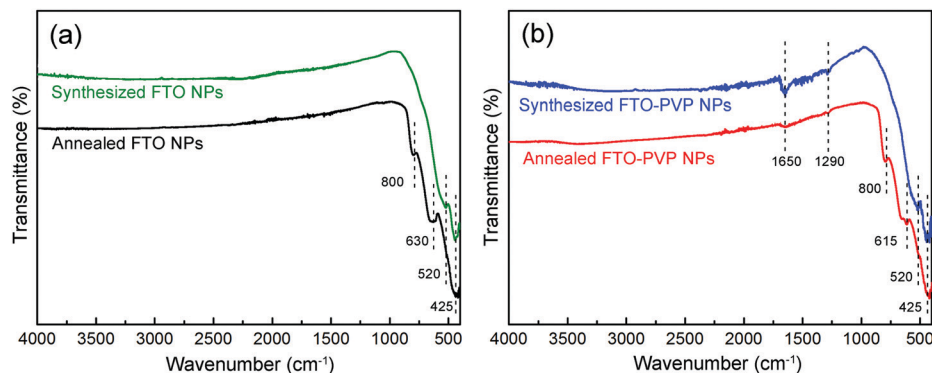


Fig. 5 FT-IR spectra for synthesized and annealed products of FTO NPs (a) and FTO-PVP NPs (b).

Based on the above results, we find that the addition of PVP not only reduces the particle size, and increases the specific surface area and pore volume of Fe₂TiO₅ NPs, but it also leads to the generation of oxygen vacancies in the lattices. The possible reason is that during the synthesis process of Fe₂TiO₅ NPs assisted by PVP, the negatively-charged carbonyl groups of PVP molecules tend to bind with the unsaturated and positively-charged Fe ions in the Fe₂TiO₅, leading to the generation of oxygen vacancies. Similar phenomena have been reported for the PVP-assisted synthesis of TiO₂ NPs,¹⁰ CeO₂ NPs,¹¹ MoO₃ nanosheets,¹² and BiOBr nanosheets.¹³

To explore the differences of the structural stability between FTO NPs and FTO-PVP NPs, extensive *in situ* irradiation experiments were carried out. To better observe the irradiation effect, all the TEM images were obtained at a high electron beam current density (more than 50 pA cm⁻²). Our experiments show that after a 5 minute irradiation, the structure and morphology of FTO NPs remain unchanged, while the morphology of FTO-PVP NPs changes significantly. Considering that the average particle size of FTO NPs is larger than that of FTO-PVP NPs, we should take the particle size effect into account. To exclude the particle size effect on the morphology change, several particles with a similar size (about 100 nm) were chosen from both samples to study their electron beam irradiation behaviors. Consistent with our previous observation, FTO NPs still show no obvious morphology changes but FTO-PVP NPs exhibit an evident morphological evolution. Therefore, the distinct morphological changes under the electron beam irradiation do not originate from the different particle sizes of the two samples.

The morphology, structure and chemical composition of FTO-PVP NPs were further investigated before and after the electron beam irradiation. Fig. 6a and c show the BF images of FTO-PVP NPs before and after the irradiation, respectively. It can be seen from Fig. 6a that the edges of FTO-PVP NPs are smooth and the boundaries between the particles are clear. However, after a 2 minute irradiation, their surfaces become rough and their edges are surrounded with many tiny particles, as displayed in Fig. 6c. From the SAED patterns obtained from the FTO-PVP NPs before and after the irradiation (Fig. 6a and c), it can be found that no phase transformation occurs. This implies that the structure of the FTO-PVP NPs remains unchanged after

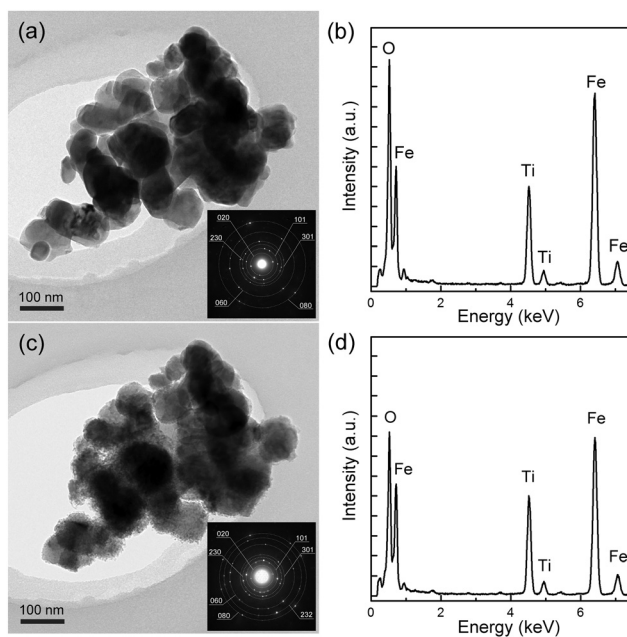


Fig. 6 Typical BF TEM images of the FTO-PVP NPs before (a) and after (c) the electron beam irradiation, respectively. Insets show the corresponding SAED patterns. EDS spectra obtained from FTO-PVP NPs before (b) and after (d) the irradiation.

the irradiation. The chemical composition of FTO-PVP NPs was investigated before and after the irradiation using EDS, as shown in Fig. 6b and d. Both spectra contain elements of Fe, Ti and O, from which a small change is found for the peak intensities of Fe and Ti, while an evident decrease is observed for the peak intensity of O after the irradiation. Table 1 summarizes the quantification results of the EDS spectra before and after the irradiation. Before the irradiation, the atomic ratio for Fe, Ti and O is about 2 : 1 : 5, which conforms to the stoichiometry of Fe₂TiO₅, while it becomes 2 : 1 : 4.43 after the irradiation. This indicates that the atomic concentration of O decreases by about 10% in the FTO-PVP NPs after the electron beam irradiation. That is to say, the electron beam induces the formation of oxygen vacancies. Therefore, the electron beam irradiation can significantly induce changes in the morphology and composition of the FTO-PVP NPs.

Table 1 Quantification results of EDS spectra for FTO-PVP NPs before and after the irradiation

Composition	Weight percentage (%)		Atomic percentage (%)		Atomic ratio	
	Before	After	Before	After	Before	After
Fe	47.20	48.10	25.90	26.70	2.09	1.98
Ti	19.60	20.90	12.40	13.50	1.00	1.00
O	33.10	30.90	61.60	59.80	4.97	4.43

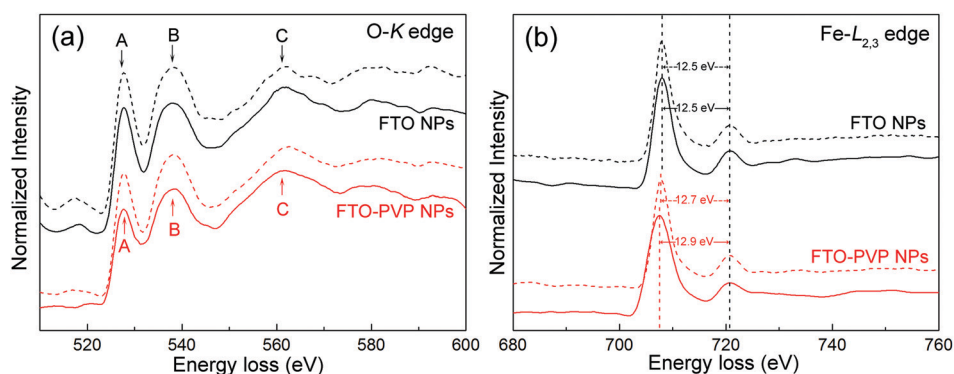
To investigate the detailed composition changes of FTO-PVP NPs and FTO NPs before and after the electron beam irradiation, EELS examinations were carried out. Fig. 7a shows the EELS spectra of O-K edge obtained from the FTO NPs and FTO-PVP NPs before and after the electron beam irradiation. It can be seen from Fig. 7a that three peaks (labeled A, B, and C) can be identified at the O-K edge. Before the irradiation, it is obvious that the intensity of peak A in the FTO-PVP NPs (red dashed line) is slightly lower than that of the FTO NPs (black dashed line). It has been reported that the decreased intensity of this peak is associated with the increase of oxygen vacancy content.^{36,37} Thus, it can be concluded that the content of oxygen vacancies is slightly higher in the FTO-PVP NPs than that in the FTO NPs before the irradiation. Moreover, the intensity of peak A in FTO-PVP NPs (red solid lines) decreases evidently after the 2 min irradiation, which is consistent with previous reports.^{36,37} Therefore, it is deduced that the content of oxygen vacancies increases in the FTO-PVP NPs after the irradiation. Fig. 7b shows the EELS spectra of Fe-L_{2,3} edge obtained from the FTO NPs and FTO-PVP NPs before and after the electron beam irradiation. At the Fe-L_{2,3} edge, the distance between L₃ and L₂ peaks is 12.5 eV for the FTO NPs before and after the electron beam irradiation, while for the FTO-PVP NPs, the distance is 12.7 eV before irradiation (red dashed line) and 12.9 eV after the irradiation (red solid line). It has been reported that the position of the L₃ line is sensitive to the valence states of the transition metal oxides.³⁸ Hence, the shift for the L₃ lines indicates that a little more Fe²⁺ ions exist in the FTO-PVP NPs after the irradiation.^{38,39} In addition, quantification of the EELS spectra shows that for the FTO NPs, the atomic ratio

of Fe and O is 2:(5.00 ± 0.02) before the irradiation and 2:(4.98 ± 0.02) after the irradiation, while for the FTO-PVP NPs, the atomic ratio of Fe and O is 2:(4.96 ± 0.02) before the irradiation and 2:(4.58 ± 0.02) after the irradiation, respectively. Therefore, no evident change can be found in the composition of the FTO NPs after 2 min irradiation, while for the FTO-PVP NPs, the content of oxygen vacancies and Fe²⁺ increases after the irradiation.

It is well known that knock-on collision and radiolysis are major mechanisms of damage that can cause the loss of an atom of a specimen in an electron microscope. Radiolysis occurs not only in biological and organic specimens, but also in inorganic materials. However, in the case of conducting materials, radiolysis is suppressed, leaving knock-on displacement as a major mechanism of damage.^{40,41} Fe₂TiO₅ is an n-type semiconductor oxide in which the atoms are connected by covalent bonds. In addition, the oxygen atom is the lightest element in Fe₂TiO₅, and it is most likely to be displaced by the incident electrons. Therefore, the significant decrease of the oxygen content is mainly ascribed to the contribution of knock-on collisions.

Extensive time-resolved HRTEM imaging was performed to investigate the morphological evolution of one particle of FTO-PVP NPs, as shown in Fig. 8. At the beginning, a layer exfoliation process takes place (Fig. 8a-d). The exposed surfaces of the NPs peel off one layer after another in less than a minute under the electron beam irradiation, making the surface look like a “terrace”. Subsequently, local pulverization appears at the edges of some NPs as the irradiation time increases, which produces small particles with a dimension of about 5 nm (Fig. 8e and f). Consistent with the previous observation, shown in Fig. 8c, we find that the exposed surface and edge of NPs are unstable and susceptible to change under electron beam irradiation. To identify the structure of newly-formed particles, as shown in Fig. 8e, an interplanar spacing is measured to be 2.7 Å, which corresponds to the (230) lattice spacing of Fe₂TiO₅. This proves that electron beam irradiation affects the morphology and size of the FTO-PVP NPs, while their inherent structure remains unchanged.

An intriguing process was observed after the emergence of 5 nm particles, as shown in Fig. 9. A tiny particle falling from

**Fig. 7** EELS spectra of O-K (a) and Fe-L_{2,3} (b) core loss edges obtained from the FTO NPs (black) and FTO-PVP NPs (red) before (dashed lines) and after (solid lines) the electron beam irradiation.

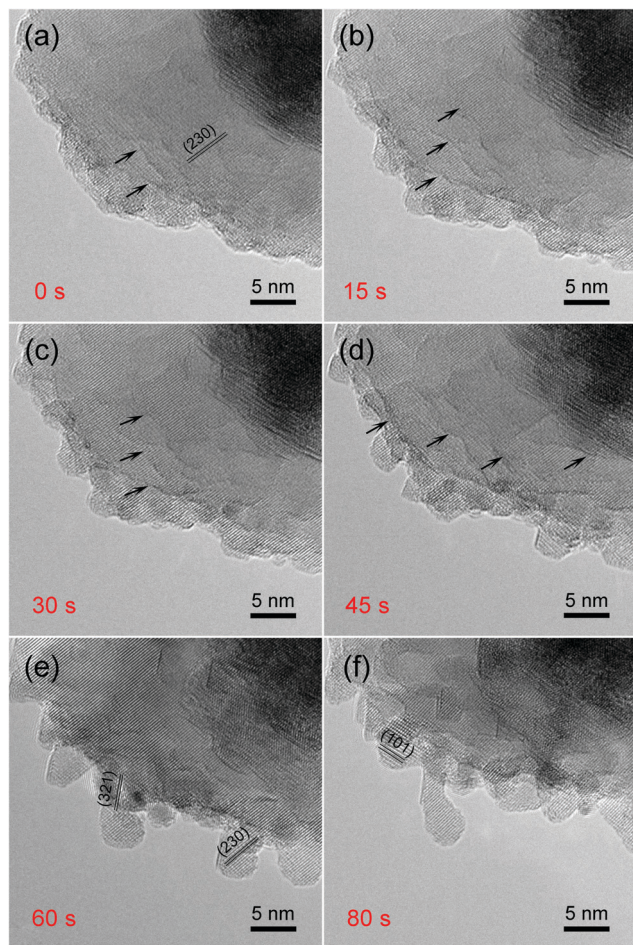


Fig. 8 Morphological evolution of FTO-PVP NPs under electron beam irradiation. (a) 0 s, (b) 15 s, (c) 30 s, (d) 45 s, (e) 60 s, and (f) 80 s.

the edge of the initial nanoparticle (NP) coalesces into the initial NP under the continuous electron beam irradiation. We measured the lattice spacings of the tiny particles before and after the coalescence, and found that no change in spacing happens, which further proves that the structure of FTO-PVO NPs does not change after the coalescence. However, most tiny particles do not undergo the coalescence process, and just fade gradually through amorphization upon prolonged electron beam irradiation (more than 5 minutes).

EELS examinations were carried out in scanning-transmission electron microscopy (STEM) mode to study the composition and elemental distribution of the damaged edge and surface of FTO-PVP NPs. Fig. 10a shows the STEM image of the damaged samples after the 2 minute electron beam irradiation, and Fig. 10b is the EELS spectrum obtained from the region enclosed by a red square (particle edge), as shown in Fig. 10a. After the irradiation, the EELS spectrum of the damaged edge of particles is consistent with that of FTO-PVP NPs except for the intensity difference of the O-K edge. Quantification of the EELS spectra shows that the atomic ratio of Fe, Ti and O is 2:1:4.58 in the FTO-PVP NPs, which is consistent with the EDS results. In addition, it can be seen that the peak shape

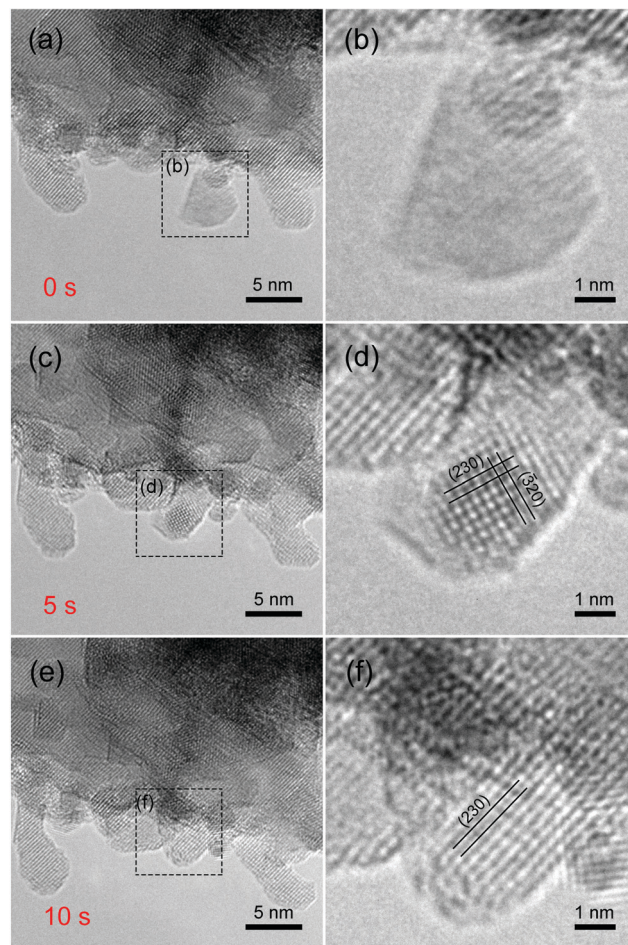


Fig. 9 HRTEM images of the coalescence process in FTO-PVP NPs. (a) 0 s, (c) 5 s, and (e) 10 s. (b, d and f) Enlarged images of the dotted regions in (a), (b) and (c), respectively.

(peak A and B) at the O-K edge of FTO-PVP NPs is quite different from that of pure TiO_2 .^{42,43} Moreover, for the Fe- $L_{2,3}$ edge, the distance between L_3 and L_2 peaks is 12.9 eV in the damaged particles, which is different from that of pure Fe (13.2 eV).^{44,45} Therefore, it can be deduced that the damaged particles are still Fe_2TiO_5 without decomposition into TiO_2 and Fe.

In our experiments, it is found that the current density of the electron beam plays an important role in the morphological evolution of FTO-PVP NPs. The morphology of the NPs hardly changes under the electron beam with a low current density (less than 20 pA cm^{-2}). However, when the electron beam current density exceeds 50 pA cm^{-2} , FTO-PVP NPs become more vulnerable, and their morphological changes occur in 15 seconds. Generally, the electron beam current density is closely related to the thermal effect and charging effect induced by the electron beam.⁴⁰ Fe_2TiO_5 is an n-type semiconductor, in which the charging effect is not common because the electrons can be quickly channeled away.⁴⁶ However, almost all the electron beam irradiation damage is accompanied by the thermal effect. Therefore, the thermal effect is dominant for the morphological evolution of the FTO-PVP NPs. From the above analysis, it is found that knock-on collision plays a dominant role in the

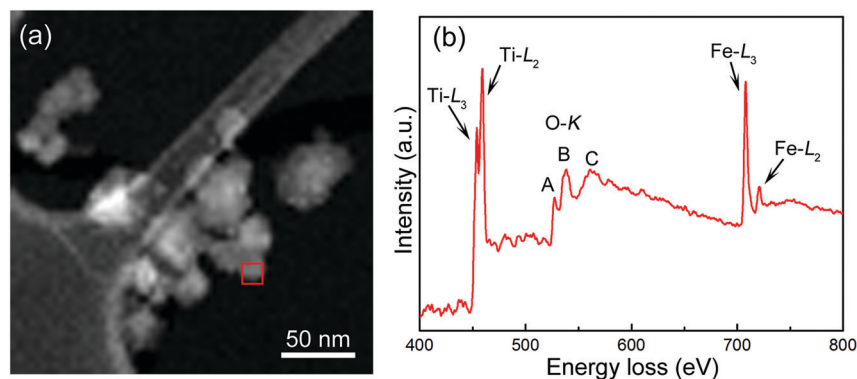


Fig. 10 (a) STEM image of FTO-PVP NPs after the 2 minute electron beam irradiation. (b) EELS spectra obtained from the region enclosed by a red square in (a).

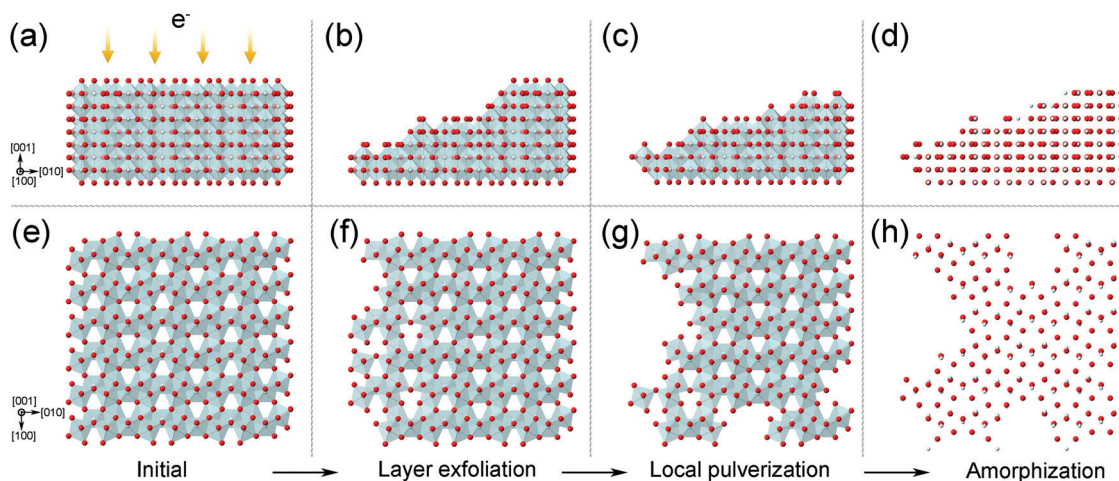


Fig. 11 Schematic diagrams of morphological evolution mechanism for the FTO-PVP NPs: (a–d) side view and (e–h) top view. Fe and Ti atoms share the blue octahedrally-coordinated sites and red balls represent oxygen atoms.

oxygen loss of the FTO-PVP NPs. Thus, it is concluded that knock-on collision and the thermal effect are the main reasons for the morphological evolution of FTO-PVP NPs.

An evolution mechanism is schematically proposed for the FTO-PVP NPs under the electron beam irradiation, as shown in Fig. 11. For the FTO-PVP NPs, oxygen vacancies are randomly generated in the interior and surface of the NPs, due to the addition of PVP in the synthesis process (Fig. 11a and e). Under the electron beam irradiation, the knock-on collision of the electrons produces more defects on the exposed surfaces, including the oxygen vacancies. Scores of electrons accumulate on the surface of particles, making the local surface temperature rise sharply. However, owing to the obstruction of the surface oxygen vacancies and residual organic compounds, heat cannot be effectively transferred, and it quickly congregates around the surfaces and defects.⁴⁷ Under the action of knock-on collision and thermal effect, the surface atomic layer becomes extremely fragile and a peeling phenomenon occurs, similar to the surface eroding in some metals. The exposed atomic surface is peeled off layer by layer, and the particles appear to form a “terrace” (Fig. 11b and f). As the irradiation

continues, the thickness of the whole particle decreases under the electron beam collision and beam-induced heating. The uneven distribution of defects and heat leads to the partial collapse of Fe_2TiO_5 lattices and local fragmentation occurs near the edges, resulting in the formation of small particles with a diameter of about 5 nm (Fig. 11c and g). With the prolongation of irradiation time, large-scale collapse of Fe_2TiO_5 lattices takes place. Eventually, most small particles undergo amorphization under the combined action of the thermal effect and collision upon further electron irradiation (Fig. 11d and h). Coalescence only takes place in a few small particles.

4. Conclusion

In conclusion, we investigate the role of PVP in the synthesis of Fe_2TiO_5 NPs and the effect of electron beam irradiation on the stability of Fe_2TiO_5 NPs produced with or without the addition of PVP. The addition of PVP not only affects the particle size, specific surface area and pore volume of Fe_2TiO_5 NPs, but also leads to the formation of oxygen vacancies in the lattices.

Due to the oxygen vacancies, FTO-PVP NPs, being not as stable as FTO NPs, undergo obvious morphological evolution under the electron beam irradiation. Three distinct morphological evolution stages, namely, layer exfoliation, local pulverization, and amorphization, result from the thermal effect and knock-on collisions caused by the incident electrons. Our work can deepen the understanding of the damage mechanism for polycrystalline oxides under the electron beam irradiation.

Conflicts of interest

There are no conflicts to declare.

Acknowledgements

The authors would like to acknowledge the financial support from High-end Foreign Experts Recruitment Programs (Grant No.: GDW20173500154 and GDW20163500110), the Shandong Province "Double-Hundred Talent Plan" (Grant No.: WST2018006), the Shandong Province High-end Foreign Experts Recruitment Program, and the Top-notch Innovative Talent Program of Qingdao City, China (Grant no.: 13-CX-8). Y. Q. Wang would also like to acknowledge the financial support from the Taishan Scholar Program of Shandong Province, China, the Qingdao International Center of Semiconductor Photoelectric Nanomaterials, and the Shandong Provincial University Key Laboratory of Optoelectrical Material Physics and Devices.

References

- 1 Q. Liu, J. F. He, T. Yao, Z. H. Sun, W. R. Cheng, S. He, Y. Xie, Y. H. Peng, H. Cheng, Y. F. Sun, Y. Jiang, F. C. Hu, Z. Xie, W. S. Yan, Z. Y. Pan, Z. Y. Wu and S. Q. Wei, *Nat. Commun.*, 2014, **5**, 5122.
- 2 P. Y. Tang, H. B. Xie, C. Ros, L. J. Han, M. Biset-Peiró, Y. M. He, W. Kramer, A. P. Rodríguez, E. Saucedo, J. R. Galán-Mascarós, T. Andreu, J. R. Morantea and J. Arbiol, *Energy Environ. Sci.*, 2017, **10**, 2124–2136.
- 3 Y. Q. Gao, Y. D. Li, G. Q. Yang, S. S. Li, N. Xiao, B. R. Xu, S. Liu, P. Qiu, S. J. Hao and L. Ge, *ACS Appl. Mater. Interfaces*, 2018, **10**, 39713–39722.
- 4 Y. X. Deng, M. Y. Xing and J. L. Zhang, *Appl. Catal., B*, 2017, **211**, 157–166.
- 5 K. M. Min, K. S. Park, A. H. Lim, J. C. Kim and D. W. Kim, *Ceram. Int.*, 2012, **38**, 6009–6013.
- 6 S. M. Guo, S. Y. Wang, N. N. Wu, J. R. Liu, Y. X. Ni and W. Liu, *RSC Adv.*, 2015, **5**, 103767–103775.
- 7 M. V. Nikolic, M. D. Lukovic, Z. Z. Vasiljevic, N. J. Labus and O. S. Aleksic, *J. Mater. Sci.: Mater. Electron.*, 2018, **29**, 9227–9238.
- 8 F. C. Gennari, J. J. Andrade Gamboa and D. M. Pasquevich, *J. Mater. Sci.*, 1998, **33**, 1563–1569.
- 9 M. Ramezani, A. Davoodi, A. Malekizad and S. H. Mashkani, *J. Mater. Sci.*, 2015, **26**, 3957–3962.
- 10 A. U. Maheswari, K. K. Anjali and M. Sivakumar, *Solid State Ionics*, 2019, **337**, 33–41.
- 11 Q. Ma, N. Izu and Y. Masuda, *ACS Appl. Nano Mater.*, 2018, **1**, 2112–2119.
- 12 Y. Wu, H. Wang, W. G. Tu, S. Y. Wu and J. W. Chew, *Appl. Organomet. Chem.*, 2019, **33**, e4780.
- 13 X. L. Xue, R. P. Chen, H. W. Chen, Y. Hu, Q. Q. Ding, Z. T. Liu, L. B. Ma, G. Y. Zhu, W. J. Zhang, Q. Yu, J. Liu, J. Ma and Z. Jin, *Nano Lett.*, 2018, **18**, 7372–7377.
- 14 X. M. Gao, M. W. Li, Y. L. Hou and C. Y. Wang, *Mater. Res. Innovations*, 2015, **19**, 1–6.
- 15 H. D. Ngo, T. D. Ngo, A. Tamanai, K. Chen, N. T. Cuong, O. S. Handegard, A. Pucci, N. Umezawa, T. Nabatame and T. Nagao, *CrystEngComm*, 2019, **21**, 34–40.
- 16 N. Kumagai, T. Hiraki, U. B. Pal, E. Kasai and T. Nagasaka, *Metall. Mater. Trans. B*, 2018, **49**, 2278–2284.
- 17 D. S. Humphrey, C. L. Pang, Q. Chen and G. Thornton, *Nanotechnology*, 2019, **30**, 025303.
- 18 C. Davoisne and H. Leroux, *Nucl. Instrum. Methods Phys. Res., Sect. B*, 2006, **243**, 371–376.
- 19 A. G. Nasibulin, L. T. Sun, S. Hämäläinen, S. D. Shandakov, F. Banhart and E. I. Kauppinen, *Cryst. Growth Des.*, 2010, **10**, 414–417.
- 20 X. Li, S. B. Cheng, S. Q. Deng, X. L. Wei, J. Zhu and Q. Chen, *Sci. Rep.*, 2017, **7**, 40911.
- 21 X. F. He, T. Xu, X. F. Xu, Y. J. Zeng, J. Xu, L. T. Sun, C. R. Wang, H. Z. Xing, B. H. Wu, A. J. Lu, Q. Q. Liu, X. S. Chen and J. H. Chu, *Sci. Rep.*, 2014, **4**, 6544.
- 22 P. P. Shanbogh, V. C. Petwal, J. Dwivedi, A. Rao and N. Sundaram, *J. Phys. Chem. C*, 2019, **123**, 10881–10892.
- 23 H. Yang, Z. H. Chi, F. Y. Li, C. Q. Jin and R. C. Yu, *Phys. Rev. B: Condens. Matter Mater. Phys.*, 2006, **73**, 024114.
- 24 Z. J. Yang, M. Walls, I. Lisiecki and M. P. Pileni, *Chem. Mater.*, 2013, **25**, 2372–2377.
- 25 T. W. Kim, J. W. Shin, J. Y. Lee, J. H. Jung, J. W. Lee, W. K. Choi and S. Jin, *Appl. Phys. Lett.*, 2007, **90**, 051915.
- 26 W. S. Pereira, J. Andrés, L. Gracia, M. A. San-Miguel, E. Z. Silva, E. Longo and V. M. Longo, *Phys. Chem. Chem. Phys.*, 2015, **17**, 5352–5359.
- 27 M. Assis, M. C. Oliveira, T. R. Machado, N. G. Macedo, J. P. C. Costa, L. Gracia, J. Andrés and E. Longo, *J. Phys. Chem. C*, 2019, **123**, 5023–5030.
- 28 J. J. Zou, B. Liu, H. Q. Liu, Y. H. Ding, T. Xin and Y. Q. Wang, *Mater. Res. Bull.*, 2018, **107**, 468–476.
- 29 Y. H. Ding, B. Liu, J. J. Zou, H. Q. Liu, T. Xin, L. H. Xia and Y. Q. Wang, *Mater. Res. Bull.*, 2018, **106**, 7–13.
- 30 D. N. Pei, L. Gong, A. Y. Zhang, X. Zhang, J. J. Chen, Y. Mu and H. Q. Yu, *Nat. Commun.*, 2015, **6**, 8696.
- 31 W. Jiang, K. L. Lai, H. Hu, X. B. Zeng, F. Lan, K. X. Liu, Y. Wu and Z. W. Gu, *J. Nanopart. Res.*, 2011, **13**, 5135–5145.
- 32 T. Yamashita and P. Hayes, *Appl. Surf. Sci.*, 2008, **254**, 2441–2449.
- 33 B. Pal, M. Sharon and G. Nogami, *Mater. Chem. Phys.*, 1999, **59**, 254–261.
- 34 K. M. Koczkur, S. Mourdikoudis, L. Polavarapu and S. E. Skrabalak, *Dalton Trans.*, 2015, **44**, 17883–17905.

- 35 Y. K. Du, P. Yang, Z. G. Mou, N. P. Hua and L. Jiang, *J. Appl. Polym. Sci.*, 2006, **99**, 23–26.
- 36 C. Wang, Y. Q. Wang, X. H. Liu, H. W. Yang, J. R. Sun, L. Yuan, G. W. Zhou and F. Rosei, *Nanotechnology*, 2016, **27**, 035702.
- 37 M. Nord, P. E. Vullum, I. Hallsteinsen, T. Tybell and R. Holmestad, *Ultramicroscopy*, 2016, **169**, 98–106.
- 38 D. H. Pearson, B. Fultz and C. C. Ahn, *Appl. Phys. Lett.*, 1988, **53**, 1405–1407.
- 39 L. Yao, S. Majumdar, L. Äkäslompolo, S. Inkinen, Q. H. Qin and S. V. Dijken, *Adv. Mater.*, 2014, **26**, 2789–2793.
- 40 R. F. Egerton, *Microsc. Res. Tech.*, 2012, **75**, 1550.
- 41 R. F. Egerton, R. McLeod, F. Wang and M. Malac, *Ultramicroscopy*, 2010, **110**, 991–997.
- 42 M. Yoshiya, I. Tanaka, K. Kaneko and H. Adachi, *J. Phys.: Condens. Matter*, 1999, **11**, 3217–3228.
- 43 K. Z. Qi, R. Selvaraj, T. A. Fahdi, S. A. Kindy, Y. Kim, G. C. Wang, C. W. Tai and M. Sillanpää, *Appl. Surf. Sci.*, 2016, **387**, 750–758.
- 44 C. Colliex, T. Manoubi and C. Ortiz, *Phys. Rev. B: Condens. Matter Mater. Phys.*, 1991, **44**, 402–411.
- 45 A. R. Liu and W. X. Zhang, *Analyst*, 2014, **139**, 4512–4518.
- 46 I. G. Gonzalez-Martinez, A. Bachmatiuk, V. Bezugly, J. Kunstmann, T. Gemming, Z. Liu, G. Cuniberti and M. H. Rummeli, *Nanoscale*, 2016, **8**, 11340–11362.
- 47 D. E. Diaz-Droguett, A. Zuniga, G. Solorzano and V. M. Fuenzalida, *J. Nanopart. Res.*, 2012, **14**, 679.